JOURNAL OF SPACECRAFT AND ROCKETS
Vol. 43, No. 4, July–August 2006

Aerodynamic Stability of Reentry Heat Shield Shapes for a Crew Exploration Vehicle

Joshua E. Johnson,* Ryan P. Starkey,† and Mark J. Lewis‡
University of Maryland, College Park, Maryland 20742

A parametric study of the static stability of blunt-body reentry heat shield geometries applicable to a crew exploration vehicle has been performed. Performance trends are identified by varying geometric parameters that define a range of cross sections and axial shapes. Cross sections considered include oblate and prolate ellipses, rounded-edge polygons, and rounded-edge concave polygons. Axial shapes consist of the spherical segment, spherically blunted cone, and power law. Aerodynamic performance results that are based on a Newtonian surface pressure distribution have been verified against wind tunnel and flight data for the Apollo Command Module. Results are within 10% for aerodynamic coefficients, and trim angles of attack are computed within 1.2-deg. Stability and aerodynamic characteristics are observed to be more sensitive to changes in axial shape than changes in cross section. When uniform density is assumed, increased stability and performance are demonstrated at negative angles of attack for geometries with extremely blunt axial shapes and noneccentric cross sections. An unstable, oblate spherical segment at 20-deg angle of attack can produce a 56.1% increase in lift-to-drag ratio compared to a noneccentric stable spherical segment. Shifting the center of gravity forward by 23.5% of its length can longitudinally stabilize this shield. The elliptical cross section, followed by the rounded-edge hexagon, and then by the rounded-edge concave hexagon rendered the most stable shapes.

Nomenclature

A	=	coefficient of power law
a_1	=	semimajor axis length for superellipse, m
b	=	exponent of power law
b_1	=	semiminor axis length for superellipse, m
C	=	aerodynamic coefficient
d	=	diameter, m
e	=	eccentricity
$j_{\max}$	=	maximum mesh points in x direction
$k_{\max}$	=	maximum mesh points in ϕ direction
l	=	length of heat shield from nose to base, m
l_M	=	length of the semimajor axis of the cross section
L/D	=	lift-to-drag ratio
M_∞	=	freestream Mach number
m	=	number of sides of the superellipse in the superformula
N	=	total number of sections in which to divide the conical base
n	=	number of the section of the conical base
n_1, n_2, n_3	=	superelliptic parameters
$\hat{n}$	=	outward normal of a surface
q_∞	=	freestream dynamic pressure, Pa
r	=	base radius, m
r_n	=	nose radius for spherically blunted cone axial shape, m
S	=	surface area of cross section, m^2
S_{hs}	=	surface area of heat shield without base area, m^2
V_∞	=	freestream velocity, m/s
V_{hs}	=	volume of heat shield, m^3
v	=	exponent of superellipse equation
x, y, z	=	coordinate directions
α	=	angle of attack, deg
β	=	sideslip angle, deg
γ	=	ratio of specific heats
η_v	=	volumetric efficiency
θ_c	=	half-cone angle, deg
θ_s	=	half-spherical-segment angle, deg
ϕ	=	sweep angle, rad
ω	=	angle from x axis and in the xy plane, rad

Subscripts

A	=	axial force
cg	=	location of center of gravity
cp	=	location of center of pressure
D	=	drag
H	=	horizontal component with respect to the body
L	=	lift
l	=	rolling moment
m	=	pitching moment
N	=	normal force
n	=	yawing moment
R	=	resultant
V	=	vertical component with respect to the body
Y	=	side force
α	=	derivative with respect to angle of attack, per rad
β	=	derivative with respect to sideslip angle, per rad
0	=	location of nose, moments normalized by base diameter d

Presented as Paper 2005-4112 at the AIAA/ASME/SAE/ASEE 41st Joint Propulsion Conference, Tucson, AZ, 10–13 July 2005; received 13 September 2005; revision received 17 November 2005; accepted for publication 17 November 2005.

*Graduate Research Assistant, Department of Aerospace Engineering, 3181 Glenn L. Martin Hall; johnsje@umd.edu. Student Member AIAA.

†Research Scientist, Department of Aerospace Engineering, 3181 Glenn L. Martin Hall; rstarkey@umd.edu. Senior Member AIAA.

‡Professor, Department of Aerospace Engineering, 3181 Glenn L. Martin Hall; lewis@eng.umd.edu. Fellow AIAA.

I. Introduction

DURING planetary entry, a blunt-bodied capsule such as might be used in NASA's crew exploration vehicle (CEV) will require the proper combination of aerodynamic performance, stability, and heat transfer to follow its trajectory successfully while ensuring passenger safety. A CEV on trajectory from the moon or Mars will reenter Earth's atmosphere at high hypersonic velocities, with projected Mach numbers ranging from 30 to 50, with associated high heat loads along the frontal surface. The Apollo Command Module

(CM),[1] designed for a similar lunar mission, used a simple spherical ablative heat shield along its frontal surface to absorb and dissipate these heat loads, and the general stability of this design was determined by the heat shield's aerodynamic characteristics.

The generic space capsule[2–6] today is covered with thermal protection material, with an additional stronger heat shield on the surface of the vehicle that faces the freestream. The heat shield is designed to protect most of the vehicle from entry temperatures, and because most of the flow separates from the vehicle past the heat shield, its geometry defines most of the capsule's hypersonic aerodynamic performance. The design of the CEV also provides passive protection from entry flow disturbances that could destabilize the vehicle and endanger the astronauts, and active protection from rolling is also provided on human planetary entry vehicles with a reaction control system (RCS). The passive protection is acquired through the aerodynamic design of the heat shield, and it is common during an initial analysis for aerodynamic performance and stability requirements to be satisfied mostly through the design of a vehicle's heat shield.

Previous work has been reviewed to provide an overview on heat shield shapes. The two primary classes of shapes that have been developed are the spherical-segment[7] and the spherically blunted cone.[8,9] Extensive research on spherical segments led to its use as the heat shield shapes for the Gemini[10] and Apollo missions.[1] Likewise, the spherically-blunted cones were used on the Viking[8,11] and Pathfinder[12–14] missions to Mars.

It is not clear that a spherical shield or the classic spherically blunted coneis in fact the optimal configuration from the standpoint of aerodynamic performance and thermal survivability.[14–16] Using a simple parametric formulation in this work, we explore a wide range of possible geometries for blunt-body reentry. The aerodynamic static stability and performance of both spherical and nonspherical heat shield shapes are analyzed using Newtonian impact theory to calculate the surface pressure distributions.[17–19] Dynamic stability is not investigated in this analysis. The center of gravity for a uniform density volume is assumed to determine static longitudinal, directional, and roll stability of studied shapes. In addition to varying values of geometric parameters, angle of attack is varied to study its effects on stability derivatives and the center of pressure location.

Follow-up work will include using this code as part of a routine for optimization of heat shield shapes for controllability, drag performance, and heat survivability. Note that these shapes can also be applied to future soft shell reentry systems including inflatable aeroshell devices.

II. Geometry Generator

Because a majority of the hypersonic aerodynamic performance for a reentry capsule is defined by the design of its heat shield, several heat shield geometries are considered to determine the range of performance available for a blunt-body CEV and also to determine the geometric features that improve aerodynamic performance.

The aerodynamic analysis of each heat shield is completed by using modified Newtonian flow in a general shape aerodynamics code developed for this research. It will be shown that a modified Newtonian surface pressure distribution is acceptable for estimating the aerodynamic performance of the Apollo CM at high planetary entry velocities and trim angles of attack, for both entry from Earth orbit and from lunar return.[20,21] It thereby should be acceptable for an initial analysis of other hypersonic blunt-body shapes.

A. Heat Shield Shapes

Each heat shield in this work is defined by two geometries: the base cross section of the heat shield and the axial shape that is swept about the central axis and modified to match the base cross section. Because future work will use these shapes in optimization, an equation that produces a wide, continuous range of cross sections is ideal and available using the superformula[22] of the superellipse. The typical superellipse[23] is a curve that can transform a parallelogram into an ellipse with the Cartesian equation

$$|x/a_1|^v + |y/b_1|^v = 1 \tag{1}$$

The superformula equation[22] of the superellipse is a more generalized equation that can transform a polygon into an ellipse and then into a rounded-edge concave polygon. It defines the cross-sectional radius for $0 \le \phi \le 2\pi$,

$$r(\phi) = \left[\left|\cos\left(\tfrac{1}{4}m\phi\right)\Big/a_1\right|^{n_2} + \left|\sin\left(\tfrac{1}{4}m\phi\right)\Big/b_1\right|^{n_3}\right]^{-1/n_1} \tag{2}$$

in which m corresponds to the number of sides of a polygon, n_1 and n_2 are modifiers, and n_3 is set equal to n_2 to produce sharp or rounded-edge polygons. In the present work, n_2 was set to 1, and then Eq. (2) was applied to find values of n_1 that produced sharp-edged, nonconcave polygons. Corresponding values of n_2 for rounded-edge polygons were then determined. Because of the increased heat transfer that would be produced on sharp edges, zero radius-of-curvature polygons were not considered. Setting $n_2 = 2$ produces an ellipse; increasing n_2 beyond 2 will produce concavity in the shape. Table 1 presents the values for m, n_1, n_2, and n_3 to produce rounded-edge polygons, both straight and concave.

The cross sections in this analysis include polygons ranging from 4 to 10 sides. Once m and n_1 are set, n_2 can be varied to transform a polygon into an ellipse and then into a concave polygons, in which $n_3 = n_2$. With the parameters in Table 1, the cross sections in Fig. 1 can be constructed. If a rounded-edge pentagon is constructed, as shown in Fig. 1d, then n_2 can be increased to 2 to produce the

Table 1 Superformula parameters for rounded-edge polygons, $n_3 = n_2$

m	n_1	n_2	n_2 (concave)
4	1.00	1.50	4.0
5	1.75	1.50	4.0
6	2.30	1.50	4.0
7	3.20	1.50	5.0
8	4.00	1.40	6.0
9	5.50	1.40	6.0
10	7.00	1.40	7.0

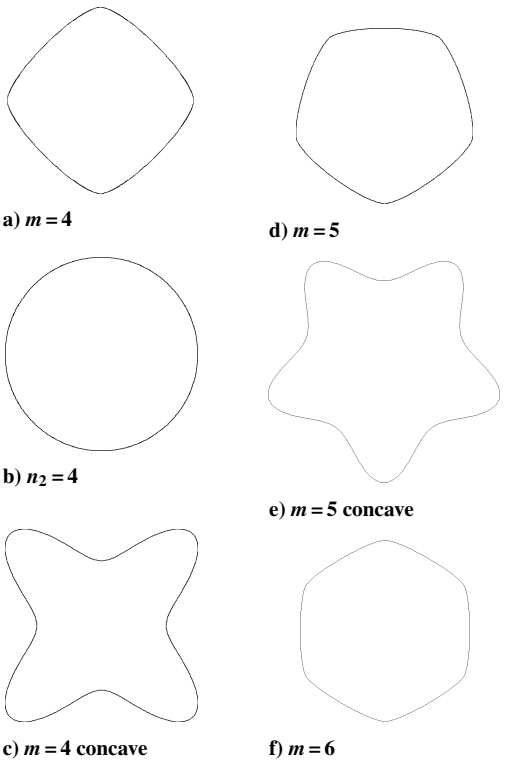

Fig. 1 Cross sections produced from Table 1.

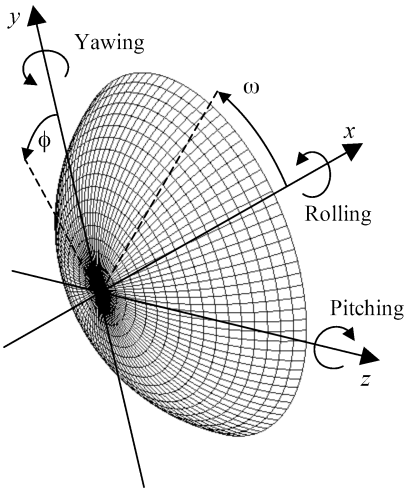

Fig. 2 Spherical-segment, $\omega = 30$ deg, $\theta_s = 60$ deg, and $n_2 = n_3 = 2$.

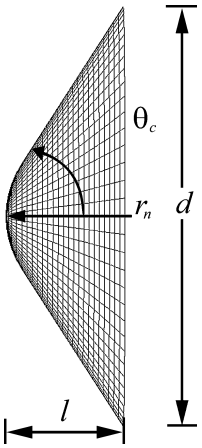

Fig. 3 Spherically blunted cone axial shape, $r_n/d = 0.25$ and $\theta_c = 60$ deg.

corresponding ellipse in Fig. 1b, and then n_2 can be increased to 4 to produce the rounded-edge concave pentagon in Fig. 1e. Note that the superformula reflects the shapes made by $n_2 > 2$ about the horizontal axis, and to keep consistency in this parametric analysis, when varying n_2, the reflection was removed.

Once the cross section is chosen, the shape of the heat shield that protrudes from the base is chosen. For this paper, this is called the axial shape to differentiate easily the protruded shape from the cross section. Three axial shapes are considered: the spherical segment, the spherically blunted cone, and the power law shape. To generate a heat shield geometry, a cross section of the axial shape is produced based on geometric input parameters, and then it is swept 360 deg about the central body axis with Eq. (2) to render the chosen base cross section.

The spherical segment is a section of a sphere that is encompassed by the angle θ_s, in which $\omega = 90$ deg $- \theta_s$. In Fig. 2, the spherical-segment cross section has been swept 360 deg about the x axis according to the chosen superelliptic base of $n_2 = n_3 = 2$. The coordinate system for this work is included in Fig. 2, including the angle $\omega = 90$ deg $- \theta_s$ and conventional directions for positive moments. One change from convention that is not shown occurs when $C_{L,V} < 0$, in which the direction of the positive rolling moment switches for a negative $C_{l,\beta}$ to still indicate a statically roll stable shape. An explanation of the sign reversal is included in the stability section of this paper. The spherically blunted cone is a cone frustum with a semivertex angle θ_c, shown in Fig. 3, and a spherically shaped blunt nose that can be varied in size according to the ratio of nose radius r_n to base diameter d. Both parameters are shown with the 60-deg spherically blunted cone in Fig. 3. Thus, it has two parts to its cross section, a spherical nose and the conical body. The cross section of the spherical nose is generated by producing

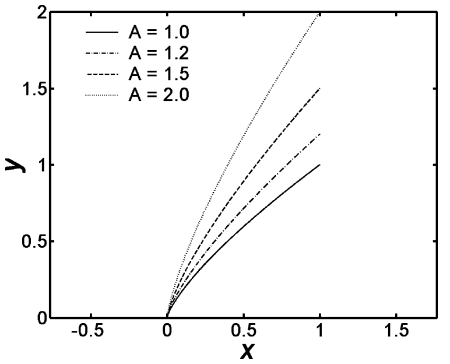

a) Cross sections of power law varying A, $b = 0.75$

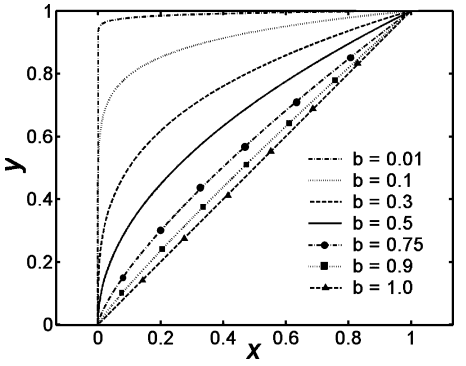

b) Cross sections of power law varying b, $A = 1$

Fig. 4 Power law axial shape.

a spherical segment with $\theta_s = \pi/2 - \theta_c$ to provide slope continuity from the spherical nose to the conical body. The spherically blunted cone cross section in the xy plane is generated with the system of equations

$$x = \begin{cases} r_n(1 - \cos\omega), & 0 \le \omega < \theta_s \\ r_n(1 - \cos\omega - \sin\omega) + y/\tan\theta_c, & \omega = \theta_s \end{cases} \tag{3}$$

$$y = \begin{cases} r_n \sin\omega, & 0 \le \omega < \theta_s \\ r_n \sin\omega + \left[\left(\frac{1}{2}d - r_n \sin\omega\right)/N\right]n, & \omega = \theta_s, \quad 0 \le n \le N \end{cases} \tag{4}$$

and the spherical segment is produced using only the first equation for x and y with $0 \le \omega \le \theta_s$. The power law cross section is generated through the equation $y = Ax^b$. The power law equation offers axial shapes with a wide range of bluntness controlled by coefficient A and exponent b, shown in Figs. 4a and 4b, respectively.

B. Implementation of Modified Newtonian Theory

Once the heat shield geometry is generated, its aerodynamic characteristics are calculated based on a modified Newtonian surface pressure distribution. Newtonian theory assumes that a particle's momentum that is normal to the surface is destroyed when it impinges on the face, whereas its tangential momentum is conserved.[17–19,24] Simple Newtonian theory is equivalent to the limit of exact oblique shock theory as M_∞ approaches infinity and γ approaches one. This work is currently being applied to Earth entry by assuming $\gamma = 1.4$, and a similar analysis can be applied to a Martian atmosphere of CO_2 by assuming $\gamma = 1.3$.

Modified Newtonian theory accounts for a maximum pressure coefficient $C_{p,\max}$ at the stagnation point, according to the Rayleigh pitot tube formula (see Ref. 25), which is a function of M_∞ and γ. The expression for the modified Newtonian pressure coefficient[17] is

$$C_p = C_{p,\max}(\boldsymbol{V}_\infty \cdot \hat{n}/V_\infty)^2 \tag{5}$$

for $\boldsymbol{V}_\infty \cdot \hat{n} < 0$, and $C_p = 0$ for $\boldsymbol{V}_\infty \cdot \hat{n} \ge 0$, in which the surface is in the aerodynamic shadow region. Because Newtonian theory allows

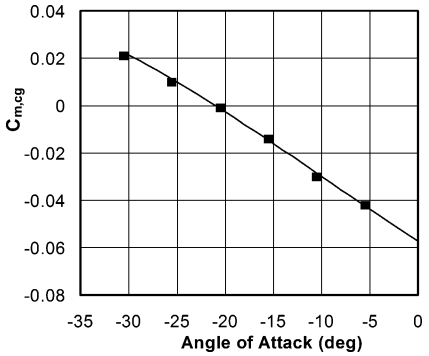

Fig. 5 Validation of $C_{m,\mathrm{cg}}$, $M = 6$: ——, modified Newtonian and ■, WT data.

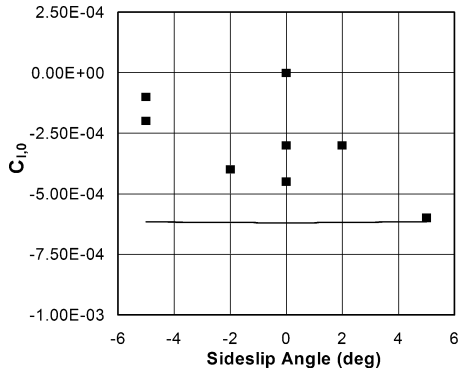

Fig. 6 Validation of $C_{l,0}$, $M = 6$: ——, modified Newtonian and ■, WT data.

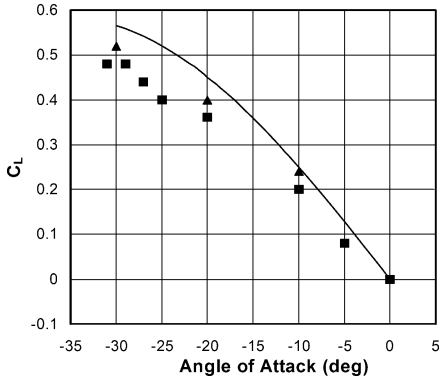

Fig. 7 Validation of C_L: ——, modified Newtonian; ■, $M = 15.8$ WT; and ▲, $M = 18.73$ WT.

aerodynamic performance to be determined within a fraction of a second of computation time, it has been chosen over more complicated, time-intensive methods for future work regarding the optimization of reentry heat shield shapes based on a stability derivative, L/D, or combination of terms.

Results from the code that applies modified Newtonian theory have been compared to wind-tunnel[26,27] and flight-test[20,21] data from Apollo CM. Figures 5–9 show a comparison of the code's results with wind-tunnel data.

The center of gravity is offset from the central body axis to trim the Apollo CM at a specific angle of attack during reentry.[28] Different center of gravity locations were considered in wind-tunnel models during the design of the CM.[26,27,29] In Fig. 5, the center of gravity location is $X_{\mathrm{cg}}/l = 2.171$, $Y_{\mathrm{cg}}/l = 0.3158$, and $Z_{\mathrm{cg}}/l = 0.0$, according to the coordinate system in Fig. 2. Additionally, because $X_{\mathrm{cg}}/l > 1$, the center of gravity location of the CM is past the heat shield. The Newtonian results for the pitching moment $C_{m,\mathrm{cg}}$ at $M_\infty = 6$ in Fig. 5 produce $C_{m,\mathrm{cg},\alpha} = -0.16$/rad and follow the behavior and closely agree with the values of the Apollo wind tunnel (WT) data.[26] Note that all moment coefficients are defined as the ratio of the moment to $q_\infty S l_M$, in which l_M is defined as the length of the semimajor axis. This definition of l_M makes it possible for the yawing moment coefficient $C_{n,0}$ at a given sideslip angle (the condition $\beta_1 \neq 0$ and $\alpha_1 = 0$) for a prolate shape $e_1 > 0$ to be equivalent to the pitching moment coefficient $C_{m,0}$ at a given angle of attack (the condition $\alpha_2 = \beta_1$, $\beta_2 = 0$, and $e_2 = -e_1$). This definition was chosen over defining l_M as the span of the heat shield.

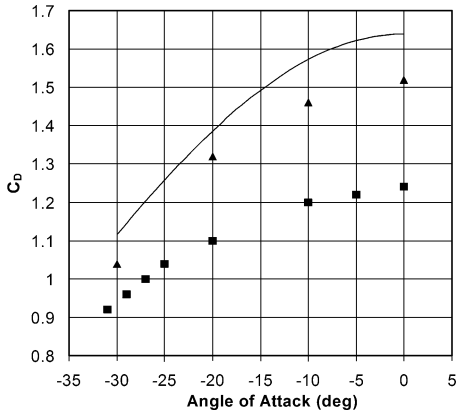

Fig. 8 Validation of C_D: ——, modified Newtonian; ■, $M = 15.8$ WT; and ▲, $M = 18.73$ WT.

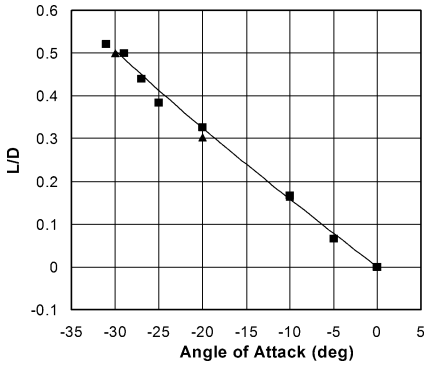

Fig. 9 Validation of L/D: ——, modified Newtonian; ■, $M = 15.8$ WT; and ▲, $M = 18.73$ WT.

The WT data for the rolling moment C_l were scattered near zero and have values that are two orders of magnitude smaller than those measured for C_m. Although the data accuracy of C_l and C_m is not reported for these WT data, the scattering and smaller values of the C_l data points in Fig. 6 suggest that the measurement instruments did not have the precision required to obtain a clear data set of the CM's rolling moment behavior. The WT data suggest a neutrally stable spherical segment at −20-deg angle of attack, and the modified Newtonian results agree. A mesh with $j_{\max} = 121$ and $k_{\max} = 203$ has been chosen based on a grid-convergence study, and the rolling moment C_l results were calculated from the Newtonian-derived C_N and C_Y values.

Because the Apollo CM is axisymmetric, the yawing moment coefficient $C_{n,0}$ at a given sideslip angle (the condition $\beta_1 \neq 0$ and $\alpha_1 = 0$) would be equivalent to the pitching moment coefficient $C_{m,0}$ at a given angle of attack (the condition $\alpha_2 = \beta_1$ and $\beta_2 = 0$). The modified Newtonian results in Figs. 7–9 were set to $M_\infty = 18.73$, but the difference between these results and those at $M_\infty = 15.8$ is negligible (0.05% difference at $\alpha = -20$ deg). Modified Newtonian results for the lift and drag coefficients are larger than values from both datasets shown in Figs. 7 and 8. However, the increase in lift and drag with an increase in Mach number in the WT data is more significant than expected; this may suggest the presence of significant WT effects. At $M_\infty = 18.73$, C_L and C_D from Newtonian theory are at most 9.6 and 7.2% larger than WT data, respectively, and they are within the uncertainty of the WT data of ±0.114 for C_L and ±0.10 for C_D (Ref. 26). L/D Newtonian results shown in Fig. 9 agree more with the WT data than C_L and C_D.

Table 2 Comparison of Apollo 4 data and computations, $M_\infty = 30$ and $\alpha = -25$ deg at 30,040 s

Parameters	Apollo 4[a]	Modified Newtonian	% Error
C_N	−0.11	−0.06387	−41.9
C_A	1.32	1.400	6.1
C_L	0.45	0.5337	18.6
C_D	1.25	1.296	3.7
L/D	0.37	0.4119	11.3

[a]Reference 21.

Compared to flight data for Apollo 4 at $M_\infty = 30$, Newtonian theory produces a C_D that is 3.7% larger, and a C_L that is 18.6% larger, as shown in Table 2.[21] According to Hillje,[21] the best flight-derived data for C_N (near maximum freestream dynamic pressure) has an uncertainty of ±0.048. Because the normal force coefficient has a small magnitude, small precision errors in C_N strongly affect the calculation of C_L. The contribution of C_N to C_L is one order of magnitude less than the contribution of C_A to C_L. However, the contribution of C_N to C_D is two orders of magnitude less than the contribution of C_A to C_D, and so an error in C_N will not affect C_D as much as C_L. This produces significant increase in accuracy of the Newtonian results for C_D at 3.7% compared to C_L at 18.6%.

Additionally, Newtonian theory produces results that trim the CM within 1.2 deg for both Apollo missions AS-202 ($\alpha = 17.5 \pm 0.5$ deg) (Ref. 20) and Apollo 4 ($\alpha = 25.5 \pm 3$ deg) (Ref. 21). For all of these reasons, it is concluded that the C_N flight data are probably inaccurate, rendering the higher percentage errors in C_L and L/D. Because the percentage differences between the theory and the acceptable CM experimental WT and flight data are less than 10%, and because the theory follows the behavior of the WT data, modified Newtonian flow is considered acceptable for comparing the basic hypersonic aerodynamic characteristics of the investigated blunt-body heat shield shapes with low computational time.

The analysis code has four main components to produce heat shield characteristics: 1) the blunt-body shape generator, 2) the aerodynamics estimator, 3) the center of gravity locator, and 4) the static stability calculator. Given the geometric parameters of a chosen base and axial shape, the shape generator produces a three-dimensional mesh of the heat shield geometry. The aerodynamics estimator determines the aerodynamic characteristics of a given shape based on modified Newtonian theory at a given angle of attack, sideslip angle, and Mach number. The aerodynamics estimator is acceptable for determining blunt-body shape hypersonic aerodynamics at fine mesh sizes with extremely low run times (usually a fraction of a second for a $j_{\max} = 121$ and $k_{\max} = 203$ mesh). It applies a third-order-accurate Runga–Kutta integration method to determine the aerodynamic characteristics and center of gravity location. The center of pressure location is then determined. The center of gravity locator can either assume a uniform density volume or pass on a given center of gravity location to the stability calculator. The static stability calculator uses the aerodynamics in conjunction with the location of the center of gravity to determine the moment coefficients about the center of gravity and the pitch, yaw, and roll stability derivatives. In future work, an optimization will be performed over a variety of shapes by having an optimizer such as Design Optimization Tools (DOT)[30] vary geometric and aerodynamic input parameters.

C. Blunt-Body Static Stability Theory

One of the assumptions of aircraft stability, $C_L \gg C_D$, cannot be followed in a blunt-body analysis because blunt bodies usually have an $L/D < 1$. The assumption of $C_L \gg C_D$ leads to the conclusion that the center of gravity must lie in front of the aircraft's neutral point (or the vehicle's center of pressure) to satisfy the requirement of $C_{m,\mathrm{cg},\alpha} < 0$ for longitudinal static stability.[31] Because this assumption does not apply to blunt bodies, it may be possible to produce longitudinal static stability with the center of pressure in front of the center of gravity. From Newtonian results for $C_{m,\mathrm{cg}}$ shown in Fig. 5 for $-30 \le \alpha \le 0$ deg, it is determined that the $X_{\mathrm{cp}}/l = 0.6556$ and Y_{cp}/l varied from 0.0000 to 0.5530 for a spherical segment of $\theta_s = 25$ deg with a noneccentric base. As a result, the code suggests that the Apollo CM with a $X_{\mathrm{cg}}/l = 2.171$ is one successful example of maintaining longitudinal static stability with the center of pressure in front of the center of gravity.

Similar to X_{cp}/l being constant over a range of α for a spherical segment, $e = 0$ and $\theta_s = 25$ deg, it has been proven that $X_{\mathrm{cp}}/l = 0.6667$ for a sharp cone in a Newtonian flowfield, suggesting that X_{cp}/l is independent of half-cone angle θ_c (Ref. 19). Note that not all spherical segments have $X_{\mathrm{cp}}/l = 0.6556$, but at least one does with $\theta_s = 25$ deg and $e = 0$, including the Apollo CM. The general pitching moment equation[19] that relates X_{cp} and Y_{cp} to $C_{m,0}$ is

$$C_{m,0} = -C_N(X_{\mathrm{cp}}/d) + C_A(Y_{\mathrm{cp}}/d) \tag{6}$$

in which

$$C_{m,N,0} = -C_N(X_{\mathrm{cp}}/d), \qquad C_{m,A,0} = C_A(Y_{\mathrm{cp}}/d)$$

The equations have been modified to follow the coordinate system shown in Fig. 2 that has a positive C_m corresponding to a nose-up moment. Bertin[19] notes that the axial force's contribution to the pitching moment is commonly neglected in the definition of the center of pressure location at and near zero angle of attack. However, this assumption does not apply to blunt-body aerodynamics because $C_{m,A,0}$ is commonly the dominant term for a blunt body. It usually is not the dominating term for slender bodies, in which case the resulting formula[17–19] for a circular cone at zero angle of attack $X_{\mathrm{cp}}/l = 2/(3\cos^2\theta_c)$ may apply, but this equation complicates the analysis because X_{cp}/l is constant at 0.6667 without the assumption. If that equation is applied to a blunt circular cone with $\theta_c = 70$ deg, then $X_{\mathrm{cp}}/l = 5.7$, which is not close to $X_{\mathrm{cp}}/l = 0.6667$. That formula is only close to the exact solution for small θ_c, but a blunt-body cone does not have a small θ_c. For a general blunt-body shape, the following relation[17,19] will not determine the x location of the center of pressure based on pitching moment calculations:

$$X_{\mathrm{cp}}/d \neq -C_{m,0}/C_N \tag{7}$$

Instead, X_{cp}/l for a given blunt-body shape can be determined from the normal force's contribution to the pitching moment $C_{m,N,0}$ as shown in Eq. (6). Once the center of pressure is located, the moments about the center of gravity can be determined and should match blunt-body WT data as shown in Fig. 5. Because Newtonian flow results for $C_{m,\mathrm{cg}}$ closely agree with actual values for a spherical segment $\theta_s = 25$ deg, the code can accurately predict the trim angles of attack within 1.2 deg of the flight data for both Apollo mission AS-202 ($\alpha_{\mathrm{trim}} = 17.5 \pm 0.5$ deg) (Ref. 20) and Apollo 4 ($\alpha_{\mathrm{trim}} = 25.5 \pm 3$ deg) (Ref. 21).

When either a disturbance in the flow or a control input generates a rolling moment about the center of gravity of a lift-generating vehicle, the direction of the lift vector relative the horizon is no longer perpendicular, causing the vehicle to sideslip. In general, a lift-generating vehicle sideslips as it rolls, and general stability theory concludes that there is a coupled effect that can be related to the vehicle's roll angle and the freestream sideslip angle. To make a lift-generating vehicle statically stable when it encounters a flow disturbance that brings the vehicle away from its desired orientation and path, the vehicle must be able to produce a countermoment to bring it to its initial orientation (usually zero-roll angle or the designed trim position).

Aircraft stability assumes that the lift vector is always positive for an aircraft in wings-level attitude; this leads to the standard convention that a positive rolling moment renders a positive change in sideslip. As a result, the rolling stability derivative $C_{l,\beta}$ is required to be negative for static stability to counter flow disturbances.[31] Spacecraft stability must also account for the possibility that the vehicle may be designed to produce negative lift during a portion of its trajectory. If the lift vector is negative, then a positive rolling moment renders a negative change in sideslip, producing the reverse relationship between roll angle and sideslip angle, in which a positive roll angle produces a negative sideslip angle. In this case, the rolling stability derivative $C_{l,\beta}$ is required to be positive for static

roll stability. Because a negative $C_{l,\beta}$ is commonly associated with a statically roll stable vehicle, this convention is maintained in this work by reversing the direction of the positive rolling moment convention when the vehicle produces negative lift. The sign reversal of the positive rolling moment produces the discontinuity for all roll stable configurations to have $C_{l,\beta} < 0$. As a result, if the positive rolling moment direction were to be kept constant, then there would be stable configurations with $C_{l,\beta} > 0$, and there would not be a discontinuity. With the sign reversal, the stable and unstable oblate geometries are clearly divided.

III. Results

A. Selecting Superelliptical Base

Aerodynamic results were acquired for several axial and base shape combinations with the parameters in Table 1. Because this analysis mainly concerns aerodynamic stability, one of the main considerations in choosing a polygon of m sides is for it to be passively longitudinally stable over a range of cross sections, and one of the most longitudinally stable shapes was chosen. To compare the value of the pitching moment consistently throughout the given shapes, moments about the tip of the nose are considered. Moments about the shape's center of gravity are accounted for later in this analysis. The derivative of the pitching moment coefficient $C_{m,0,\alpha}$ shown in Fig. 10 varies slightly with the rounded-edge concave m-gon compared to its variance with eccentricity. Because the hexagon has the most stable value for pitching and yawing moments, it was decided that a superellipse with $m = 6$ would be featured in this analysis. The results in this section focus on heat shield geometries with the rounded-edge and concave hexagonal ($m = 6$) and elliptical cross sections.

The $C_{m,0,\alpha}$ distribution also suggests that eccentricity always decreases longitudinal static stability for the shapes considered. Positive values of the eccentricity correspond to the prolate shapes and negative values to the oblate ones. A prolate eccentricity value of 0.5 was chosen as the constant eccentricity at which to present results because it does not considerably lower vehicle stability and because data on eccentric heat shields are scarce. Note that a particular oblate shape with a larger L/D but smaller C_L than the common noneccentric spherical segment will be discussed later in this analysis.

B. Heat Shield Shapes and Aerodynamic Performance

The results are acquired at $M_\infty = 36$, the reentry Mach number from lunar return for the trajectory of the Apollo CM. The code was run over several ranges of geometric parameter values and angles of attack for each of the axial shapes and cross sections. The set of superelliptic bases included a rounded-edge hexagon, an ellipse, and a rounded-edge concave hexagon, each with an eccentricity of 0.5 as shown in Fig. 11. Examples of axial shapes are also shown in Fig. 11. The ranges of the geometric variables for the axial shapes are included in Table 3; Table 3 has ranges that are applied to most of the analysis, including the results in Table 4. The axial shapes shown in Fig. 11 are those applied when varying α; of the three axial shapes in Fig. 10, the one with the smallest geometric l/r is

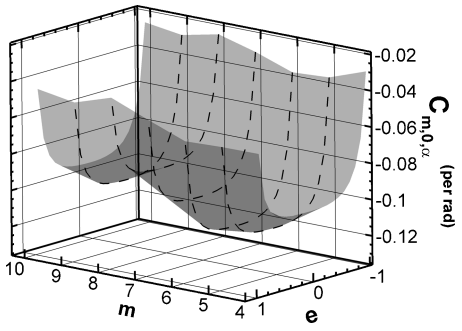

Fig. 10 $C_{m,0,a}$ distribution varying m-gon and e with spherical-segment axial shape and rounded-edge concave cross section, $\alpha = -20$ deg and $\beta = 5$ deg.

Table 3 Variable ranges and constants for each axial shape

Variable range	Constants
	Spherical segment
$-30 \le \alpha \le 0$ deg	$\theta_s = 25$ deg (Apollo CM)
$5 \le \theta_s \le 90$ deg	$\alpha = -20$ deg
	Spherically blunted cone
$-30 \le \alpha \le 0$ deg	$\theta_c = 70$ deg, $r_n/d = 0.25$ (Viking Mars Lander)
$30 \le \theta_c \le 89$ deg	$\alpha = -20$ deg, $r_n/d = 0.25$
$0.01 \le r_n/d \le 1.00$	$\alpha = -20$ deg, $\theta_c = 70$ deg
	Power law shape
$-30 \le \alpha \le 0$ deg,	$A = 2$, $b = 0.75$
$1 \le A \le 6$	$\alpha = -20$ deg, $b = 0.75$
$0.1 \le b \le 0.999$	$\alpha = -20$ deg, $A = 2$

Table 4 Effects of geometric parameters and α on aerodynamic performance[a,b]

	Spherical segment		Spherically blunted cone			Power law shape		
Parameters	α	θ_s	α	θ_c	r_n/d	α	A	b
$C_{L,V}$	5	5	5	4	1	5	5	4
L_V/D	5	5	5	3	0	5	4	3
C_m	5	5	5	5	0	5	4	1
$C_{m,\alpha}$	2	5	2	3	0	2	3	1
C_n	1	5	2	5	0	1	4	1
$C_{n,\beta}$	1	5	1	5	0	1	4	1
C_l	1	5	1	5	0	3	5	1
$C_{l,\beta}$	0	5	0	5	0	4	5	5
X_{cp}/l	0	2	0	1	1	0	3	2
Y_{cp}/l	5	3	5	1	1	5	2	1
Z_{cp}/l	0	2	1	1	1	0	1	1
η_v	N/A	4	N/A	4	1	N/A	3	1

[a]Ranges of α, θ_s, θ_c, r_n/d, A, and b given in Table 3.
[b]Percent difference key: 0, <14%; 1, 15–39%; 2, 40–75%; 3, 76–400%; 4, 401–999%; 5, 1000%+.

the spherical segment, followed by the spherically blunted cone, and then the power law shape.

As in previous work, a sideslip angle of 5 deg has been chosen in calculating the values of $C_{n,\beta}$ and $C_{l,\beta}$. Apollo 4 had a maximum sideslip of $\beta = 2$ deg, but WT tests have tested the aeroassist flight experiment[32,33] (AFE) at sideslip values up to $\beta \pm 5$ deg (Ref. 32). Note that it is convention to combine the three normal vectors C_A, C_N, and C_Y into two vectors C_L and C_D; this produces vertical and horizontal (with respect to the body axis) components of lift, represented by L_V and L_H, respectively, for cases with $\beta \neq 0$ (Refs. 20 and 21). Even though L_H is negligible in this particular analysis because β is small compared to α, L_V is listed in results with $\beta \neq 0$ to be consistent with general theory.

The coordinate system shown in Fig. 12 has the direction of positive sideslip and negative angle of attack. The direction of positive moments is shown in Fig. 2 for positive L_V. Because blunt bodies produce positive lift at negative angles of attack (for $\theta_c > 45$ deg), this analysis mainly focuses on how geometric variables vary with a constant negative angle of attack. Because the Apollo CM had trim angles of attack of -17.5 and -25.5 deg during orbital reentry and lunar return, respectively, the effects of the geometric parameters are analyzed at an angle of attack in between them at -20 deg.

C. Hypersonic Aerodynamic Performance and Stability

Figure 13 shows the effects of power law slenderness ratio A and cross-sectional parameter n_2 on $C_{m,0,\alpha}$. Figure 13 is typical of the results for all of the aerodynamic parameters in that they are much more sensitive to a change in axial shape than to a change in cross section. As a result, the effects of varying the cross section at a fixed eccentricity are not usually as important compared to the effects of changing the axial shape for longitudinal static stability. However, a cross section's eccentricity can affect the vehicle's static roll stability significantly and is discussed later in this analysis. Figure 14 shows a similar trend for $C_{m,cg,\alpha}$ but also that there is a minimum

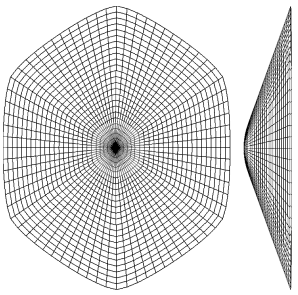

a) $n_2 = 1.5$, spherically blunted cone, $r_n/d = 0.25$ and $\theta_c = 70$ deg

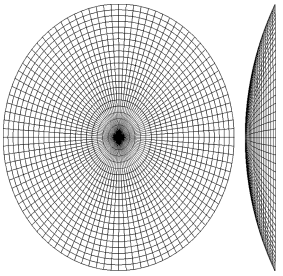

b) $n_2 = 2.0$, spherical segment, $\theta_s = 25$ deg

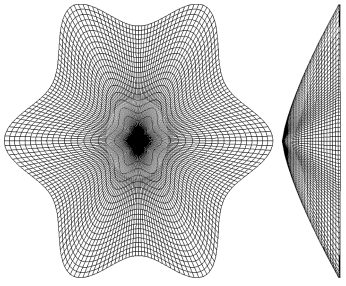

c) $n_2 = 4.0$, power law shape, $A = 2$ and $b = 0.75$

Fig. 11 Considered heat shield shapes.

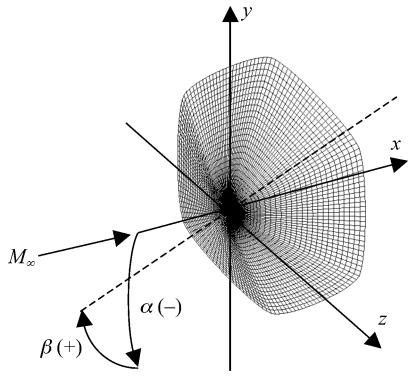

Fig. 12 Coordinate system.

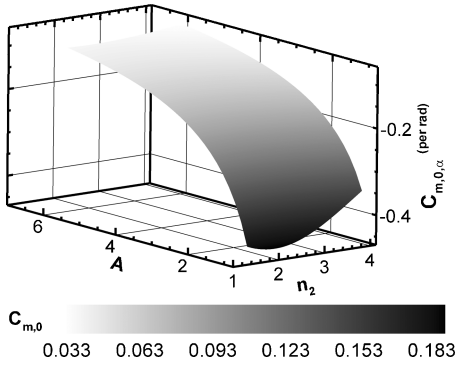

Fig. 13 $C_{m,0,\alpha}$ distribution for power law A and n_2, $b = 0.75$, $e = 0.5$, $\alpha = -20$ deg, and $\beta = 5$ deg.

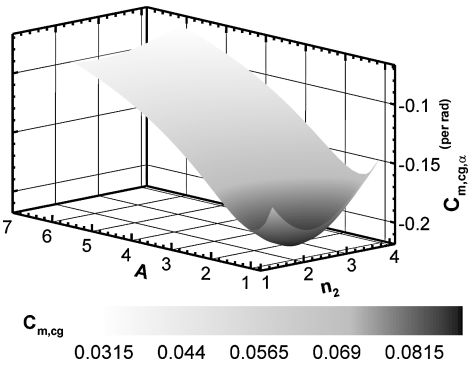

Fig. 14 $C_{m,cg,\alpha}$ distribution for power law A and n_2, $b = 0.75$, $e = 0.5$, $\alpha = -20$ deg, and $\beta = 5$ deg.

of −0.22/rad near $A = 1.5$ and $n_2 = 2$. Both $C_{m,0,\alpha}$ and $C_{m,cg,\alpha}$ have maximum absolute values at $n_2 = 2$, and this is also characteristic of the yawing moment stability derivative. The minimum $C_{m,cg,\alpha}$ may change in value and occur at a different (A, n_2) with a base of different eccentricity, or different values of b, α, or β. Because there are several combinations of variables that affect it, the process of optimization, which can vary any or all of the variables, will be an effective tool for locating extrema. This parametric analysis is conducted to determine the effects of geometric parameters on aerodynamic stability and performance. Once the effects are generally understood, optimization can be better managed to find acceptable shapes that offer an optimized stability derivative or combination of terms.

Table 4 offers a summary of the sensitivity of main aerodynamic parameters by arranging the values of percentage difference of the parameter's minimum and maximum into six groups: 0,<14%; 1, 15–39%; 2, 40–75%; 3, 76–400%; 4, 401–999%; and 5, 1000+%. Note that coefficients in category 5 have the largest percentage difference. Each group corresponds to a range of percent difference values. Because the aerodynamic parameters do not vary considerably with a change in cross section, as discussed earlier and shown in Figs. 13 and 14, the percentage differences as well as the actual values are close to each other and the same in sign when varying the cross section. As a result, Table 4 includes one column of data for the set of three base cases instead of three separate columns.

Of the three moment coefficients, only C_m varies over two orders of magnitude with α, whereas $C_{m,\alpha}$ only varies by approximately 50%. C_m also varies in two orders of magnitude with α, θ_s, θ_c, and A. In general, the moment coefficients and stability derivatives varied strongly with θ_s, θ_c, and A for the given range. For the spherically blunted cone, r_n/d only had a small effect, by varying the aerodynamic parameters ≈5–10% at most. The exponent b for the power law shape varied them ≈25%, except for $C_{l,\beta}$, which was affected strongly, although this does not necessarily mean that an extremely high value of $C_{l,\beta}$ was acquired. It only means that it varied strongly with b from a possibly negligible to significant value. As a result, a high percentage does not necessarily mean varying strongly from one significant value to another one, and some high percentages were produced because the smaller of the two absolute values was near zero ($<10^{-5}$). In the least, these results can be compared to more advanced analyses in future investigations.

A CEV probably will require a RCS to control the roll angle for human safety and follow the entry trajectory. If the rolling moment stability derivative is unstable but small, a less powerful RCS would be needed. Also, the units of the stability derivatives are per radian rather than per degree, and so reasonable rolling moment derivative and yawing moment derivative values from the AFE include $C_{l,\beta} = -0.04584/\text{rad} = -0.0008/\text{deg}$ and $C_{n,\beta} = 0.1318/\text{rad} = 0.002300/\text{deg}$ (Ref. 32). The AFE has a circular cross section with a blunted-nose, raked-cone axial shape that produces values of $C_{l,\beta}$ that are within the range of values acquired in this analysis, and the AFE's values of $C_{n,\beta}$ are within the midrange of values acquired in this analysis.

Moment coefficients and stability derivatives shown in Fig. 15 at $\alpha = -20$ deg and $\beta = 5$ deg, are affected strongly by varying the

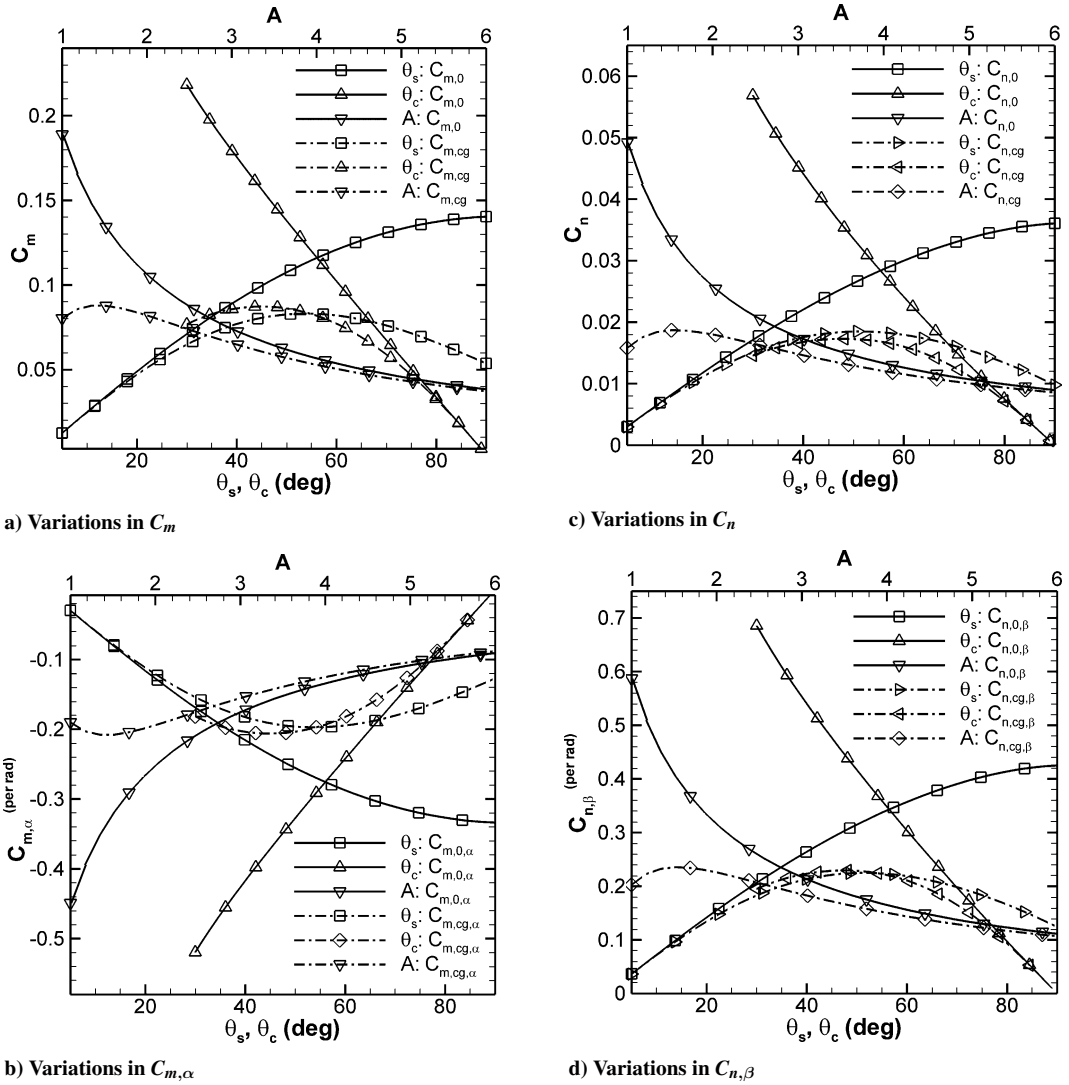

a) Variations in C_m

c) Variations in C_n

b) Variations in $C_{m,\alpha}$

d) Variations in $C_{n,\beta}$

Fig. 15 Effects of θ_s, θ_c ($r_n/d = 0.25$), and A ($b = 0.75$) on stability coefficients and derivatives, $\alpha = -20$ deg and $\beta = 5$ deg.

geometric parameters. Although the magnitudes are not equal, $C_{m,\alpha}$ in Fig. 15b would show the same behavior as that of C_m in Fig. 15a if the data were reflected about the horizontal axis. Figures 15c and 15d show C_n and $C_{n,\beta}$ have the same behavior, although C_n is an order of magnitude smaller. All four variables show that the center of gravity moments and derivatives first increase in magnitude with an increase in the geometric parameter, then produce a minimum or maximum, and then decrease in magnitude, which is a different behavior from that of the moments about the nose that usually have maximum and minimum values near or at the endpoints of the range. As a result, note that the values of the moments about the nose may neither be near the values of the moments about the center of gravity nor share the same behavior. Notice that $C_{m,\mathrm{cg}}$, $C_{m,\mathrm{cg},\alpha}$, $C_{n,\mathrm{cg}}$, and $C_{n,\mathrm{cg},\beta}$ all have maximum magnitudes near the same value, suggesting that a $C_{m,\mathrm{cg},\alpha} = -0.22/\mathrm{rad}$ for a power law shape with $A = 1.5$ would also be produced with both a spherically blunted cone of $\theta_c = 42.5$ deg and a spherical segment of $\theta_s = 52.5$ deg. Similar values can be applied to $C_{n,\mathrm{cg},\beta}$ with a maximum magnitude of 0.24/rad. Both the C_l and $C_{l,\beta}$ have values within those acquired in the WT for the AFE that are of the order of 0.01/rad for $C_{l,\beta}$ and 0.001 for C_l (Ref. 32).

Figure 16 shows how all five geometric variables affect the volumetric efficiency of the heat shields. The volumetric efficiency in this case is normalized to a hemisphere

$$\eta_v = (18\pi)^{1/3} V_{\mathrm{hs}}^{2/3} \big/ S_{\mathrm{hs}} \tag{8}$$

As a result, the most volumetrically efficient shape is the nonec-centric spherical segment at $\theta_s = 90$ deg. The volumetric efficiency is varied with eccentricity and θ_s for a range of spherical segments

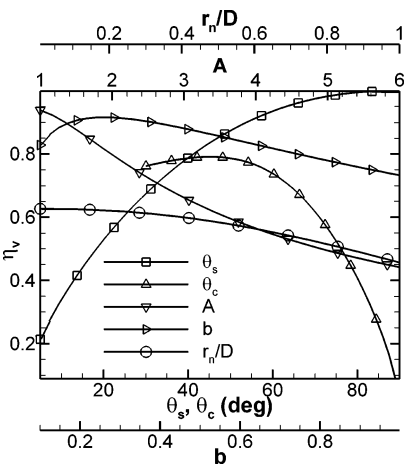

Fig. 16 Effects of θ_s, θ_c ($r_n/d = 0.25$), A ($b = 0.75$), and b ($A = 2$) on η_v, $\alpha = -20$ deg and $\beta = 5$ deg.

in Fig. 17. For $\theta_s = 90$ deg, an increase in eccentricity decreases the volumetric efficiency, but a saddle point exists at $\theta_s = 35$ deg; as a result, below $\theta_s = 35$ deg eccentricity increases the volumetric efficiency by up to 10%.

D. Effect of Eccentricity on Aerodynamic Performance

The stability derivative of the rolling moment about the center of gravity in Fig. 18 does not become significantly affected by

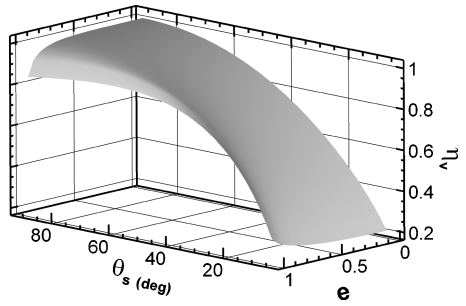

Fig. 17 Efficiency η_v distribution for spherical-segment, elliptical base, $n_2 = 2$, varying e and θ_v.

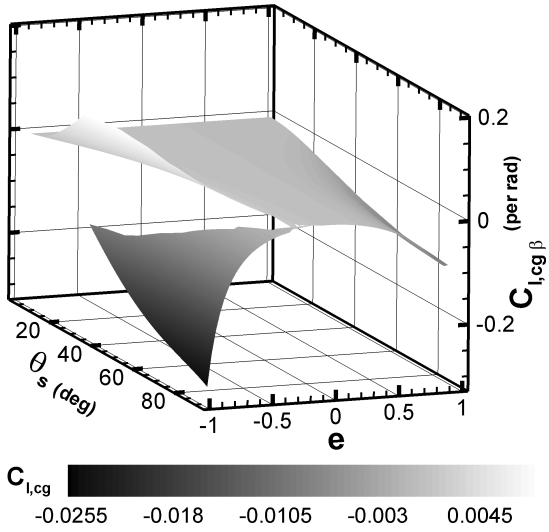

Fig. 18 $C_{l,cg,\beta}$ distribution for spherical-segment elliptical base, $n_2 = 2$, varying e and θ_s, $\alpha = 20$ deg and $\beta = 5$ deg.

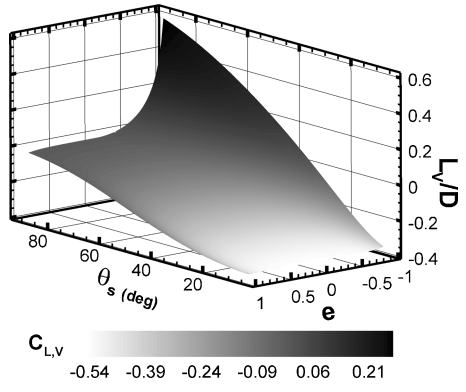

Fig. 19 L_V/D distribution for spherical-segment, elliptical base, $n_2 = 2$, varying e and θ_s, $\alpha = 20$ deg and $\beta = 5$ deg.

eccentricity until $\theta_s > 20$ deg. Beyond this value of θ_s, it is observed that the magnitude of $C_{l,cg,\beta}$ increases. For clarity purposes, the stable configurations are shown as $C_{l,cg,\beta} \leq 0$ in Fig. 18. Whereas some of the oblate shapes are stable or unstable, the noneccentric and prolate shapes ($e > 0$) are statically roll stable.

An analysis of the effect of eccentricity on L_V/D was conducted to determine whether there were any possible shapes that were not completely stable but could give a noticeable increase in L_V/D. Figure 19 shows the L_V/D distribution for varying θ_s and eccentricity. As shown in Fig. 20, a positive α data set produced the positive L_V/D value of 0.584, a 56.1% increase, at $\theta_s = 90$ deg for an oblate shape with $e = -0.95$, in which $b_1 = 1.0$ and $a_1 = 0.311$ at $\alpha = 20$

Table 5 Aerodynamic comparison of spherical segments, $\beta = 5$ deg

	$e = 0$, $n_2 = 2$		$e = -0.95$, $n_2 = 2$
Parameters	$\theta_s = 5$ deg, $\alpha = -20$ deg	$\theta_s = 25$ deg, $\alpha = -20$ deg	$\theta_s = 90$ deg, $\alpha = 20$ deg
$C_{L,V}$	0.560	0.468	0.282
L_V/D	0.374	0.335	0.584
$(L_V/D)_\alpha$	−1.10	−0.961	0.469
$C_{m,0}$	0.0126	0.0613	−0.105
$C_{m,0,\alpha}$	−0.0299	−0.145	−0.363
$C_{n,0}$	0.00302	0.0147	0.0133
$C_{n,0,\beta}$	0.0365	0.177	0.161
$C_{l,0}$	0.000	$-3.38E-5$	−0.00808
$C_{l,0,\beta}$	——	$-4.06E-5$	−0.0924
$C_{m,cg}$	0.0126	0.0575	−0.0195 (0.0310)
$C_{m,cg,\alpha}$, /rad	−0.0299	−0.136	−0.0990 (0.0566)
$C_{n,cg}$	0.00301	0.0138	0.00785 (0.00488)
$C_{n,cg,\beta}$, /rad	0.0364	0.166	0.0916 (0.0541)
$C_{l,cg}$	0.000	$-3.38E-5$	−0.00808 (−0.00808)
$C_{l,cg,\beta}$, /rad	——	$-4.06E-5$	−0.0924 (−0.0924)
X_{cg}/l	0.663	0.662	0.400 (0.635)
η_v	0.204	0.583	0.922

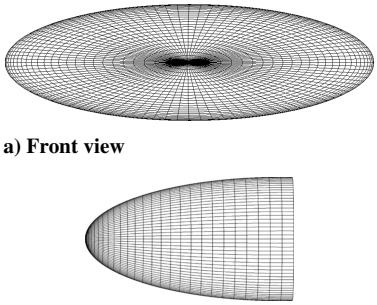

a) Front view

b) Side view

Fig. 20 Spherical segment $\theta_s = 90$ deg and $e = -0.95$, with increase of 56% in L_V/D.

deg compared to a less round, more blunt $\theta_s = 5$ deg with $e = 0.0$ with a positive L_V/D value of 0.374 at $\alpha = -20$ deg. However, $C_{L,V}$ drops to 0.282 from 0.56, a 49.6% decrease.

Table 5 lists the aerodynamic and stability characteristics based on modified Newtonian flow and uniform density heat shield geometries. The characteristics of the following geometries are listed in Table 5: $\theta_s = 5$ deg and $e = 0.0$, $\theta_s = 25$ deg and $e = 0.0$ (similar to the Apollo CM heat shield), and $\theta_s = 90$ deg and $e = -0.95$. All three have stable yawing moments also, with $\theta_s = 25$ deg and $e = 0.0$ at the largest value of 0.0138 for $C_{n,cg}$, and the other two have smaller yawing moment coefficients on the order of 0.003. Whereas the yawing moment derivative $C_{l,0,\beta}$ for $\theta_s = 5$ deg and $e = 0.0$ is only 27.7% of the $C_{l,0,\beta}$ for the AFE, both the oblate $\theta_s = 90$ deg and $e = -0.95$ and noneccentric $\theta_s = 25$ deg have values of the same order as the AFEs. The rolling moment derivative about the center of gravity for $\theta_s = 5$ deg and $e = 0.0$ is negligible, but the oblate $\theta_s = 90$ deg and $e = -0.95$ has a $C_{l,0,\beta} = -0.0924$ that is twice the stability derivative of the AFE. The volumetric efficiency is lower for the blunt shapes $\theta_s = 5$ and $\theta_s = 25$ deg with values of 0.204 and 0.583, respectively, compared to a value of 0.922 for $\theta_s = 90$ deg and $e = -0.95$. The two noneccentric cases have stable pitching moments. With the high eccentricity of $e = -0.95$ comes the unstable pitching moment derivative $C_{m,cg,\alpha} = 0.0566$/rad if a uniform density heat shield is assumed. However, if the uniform density value $X_{cg}/l = 0.635$ is switched to $X_{cg}/l = 0.400$, then the pitching moment becomes stable with $C_{m,cg,\alpha} = -0.099$/rad. In addition to values of aerodynamic moments at $X_{cg}/l = 0.400$, Table 5 includes moment and derivative values for this geometry with $X_{cg}/l = 0.635$ in parentheses. As a result, it may be advantageous to further study oblate geometries that produce higher L_V/D because an increase in trim L_V/D opens a larger range of entry flight-path angles available

for planetary entry and significantly increases the range capability of the space capsule.[1]

IV. Conclusions

An analysis of blunt-body heat shield shapes for a CEV has been conducted to determine the main effects of several geometric parameters on the aerodynamic performance and stability of the vehicle. This analysis is completed by picking a cross section and an axial shape to generate a heat shield mesh and then by placing the mesh into an aerodynamics program based on modified Newtonian flow. The results were validated with WT and flight-test data, and $C_{m,\mathrm{cg}}$ and L/D matched the values of the Apollo CM closer than the results of C_L and C_D.

Although the hexagon is the most aerodynamically stable of the polygons ($m = 4$–10), it did not have the highest L_V/D, and L_V/D became larger as n_2 approaches the elliptical cross section ($n_2 = 2$). There is a tradeoff between L_V/D and the pitching moment stability derivative, and future investigation through optimization would assist in finding the best combination of L_V/D and $C_{m,\mathrm{cg},\alpha}$. Although the increase in L_V/D of 56.1% may be beneficial by making the cross section strongly oblate at $e = -0.95$, the heat shield would be longitudinally statically unstable assuming uniform density. One way to remove this instability is by moving the center of gravity forward by 23.5% to $X_{\mathrm{cg}}/l = 0.400$.

A change in cross section did not affect the aerodynamic performance of the heat shield as significantly as a change in axial shape. A change in axial shape rendered a larger range of aerodynamic characteristics. It was also observed that the magnitudes of the longitudinal and directional stability derivatives are maximized with an elliptical base as opposed to a rounded-edge hexagonal concave base. Table 4 summarized the sensitivities of the aerodynamic parameters to the geometric parameters. C_m varied strongly with α, θ_s, θ_c, and A, whereas the other moment coefficients and stability derivatives varied strongly with θ_s, θ_c, and A. The results of $C_{l,\beta}$ are of the same order of magnitude as other blunt-body designs. For $\theta_s < 35$ deg, an increase in eccentricity from 0.0 to 0.95 increases the volumetric efficiency by up to 10%. Incorporating all of these parameters into an optimization process may assist in producing heat shield shapes with an improved combination of aerodynamic characteristics.

Acknowledgments

This research was supported by the Space Vehicle Technology Institute (SVTI), one of the NASA Constellation University Institute Projects (CUIP), under Grant NCC3-989, with joint sponsorship from the Department of Defense. Appreciation is expressed to Ken Yu, director of the SVTI at the University of Maryland, Claudia Meyer of the NASA John H. Glenn Research Center at Lewis Field, Program Manager of CUIP, and to John Schmisseur and Walter Jones of the U.S. Air Force Office of Scientific Research, the support of whom is greatly appreciated.

References

[1]Crowder, R. S., and Moote, J. D., "Apollo Entry Aerodynamics," *Journal of Spacecraft and Rockets*, Vol. 6, No. 3, 1969, pp. 302–307.

[2]Stewart, J. D., and Greenshields, D. H., "Entry Vehicles for Space Programs," *Journal of Spacecraft and Rockets*, Vol. 6, No. 10, 1969, pp. 1089–1102.

[3]Levine, P., Ellis, T. R., and Georgiev, S., "Factors Influencing the Design and Performance of Mars Entry Vehicles," *Journal of Spacecraft and Rockets*, Vol. 2, No. 2, 1965, pp. 130–146.

[4]Davies, C. B., and Park, C., "Aerodynamic Characteristics of Generalized Bent Biconic Bodies for Aero-Assisted Orbital Transfer Vehicles," NASA TM-84362, May 1983.

[5]Tauber, M., Chargin, M., Henline, W., Chiu, A., Yang, L., Hamm, K. R., Jr., and Miura, H., "Aerobrake Design Studies for Manned Mars Missions," *Journal of Spacecraft and Rockets*, Vol. 30, No. 6, 1993, pp. 656–664.

[6]Braun, R. D., "Aerodynamic Requirements of a Manned Mars Aerobraking Transfer Vehicle," *Journal of Spacecraft and Rockets*, Vol. 28, No. 4, 1991, pp. 361–367.

[7]Kruse, R. L., Malcolm, G. N., and Short, B. J., "Comparison of Free-Flight Measurement of Stability of the Gemini and Mercury Entry Capsules at Mach Numbers 3 and 9.5," NASA TM-X-957, April 1964.

[8]Kirk, D. B., Intrieri, P. F., and Seiff, A., "Aerodynamic Behavior of the Viking Entry Vehicle: Ground Test and Flight Results," *Journal of Spacecraft and Rockets*, Vol. 15, No. 4, 1978, pp. 208–212.

[9]Chrusciel, G. T., and Hull, L. D., "Theoretical Method for Calculating Aerodynamic Characteristics of Spherically Blunted Cones," AIAA Paper 1968-0674, June 1968.

[10]Faget, M. A., Garland, B. J., and Buglia, J. J., "Preliminary Studies of Manned Satellites, Wingless Configuration: Nonlifting," NACA RM L58E07a, Aug. 1958.

[11]Sammonds, R. I., and Kruse, R. L., "Viking Entry Vehicle Aerodynamic at M = 2 in Air and Some Preliminary Test Data for Flight in CO_2 at M = 12," NASA TN D-7974, June 1975.

[12]Willcockson, W. H., "Mars Pathfinder Heatshield Design and Flight Experience," *Journal of Spacecraft and Rockets*, Vol. 36, No. 3, 1999, pp. 374–379.

[13]Moss, J. N., Blanchard, R. C., Wilmoth, R. G., and Braun, R. D., "Mars Pathfinder Rarefied Aerodynamics: Computations and Measurements," AIAA Paper 98-0298, Jan. 1998.

[14]Milos, F. S., Chen, Y. K., "Mars Pathfinder Entry Temperature Data, Aerothermal Heating, and Heatshield Material Response," AIAA Paper 98-2681, June 1998.

[15]Park, C., "Aerothermodynamics of Manned Mars Missions," AIAA Paper 89-0313, Jan. 1989.

[16]Rochelle, W. C., Bouslog, S. A., and Ting, P. C., "Aerothermodynamic Environments for Mars Entry, Mars Return, and Lunar Return Aerobraking Missions," AIAA Paper 90-1791, June 1990.

[17]Rasmussen, M., *Hypersonic Flow*, Wiley, New York, 1994, Chap. 9.

[18]Regan, F., *Re-Entry Vehicle Dynamics*, AIAA Education Series, AIAA, Washington, DC, 1994, Chap. 9.

[19]Bertin, J., *Hypersonic Aerothermodynamics*, AIAA Education Series, AIAA, Washington, DC, 1993, Chap. 8.

[20]Hillje, E. R., "Entry Flight Aerodynamics from Apollo Mission AS-202," NASA TN D-4185, Oct. 1967.

[21]Hillje, E. R., "Entry Aerodynamics at Lunar Return Conditions Obtained from the Flight of Apollo 4 (AS-501)," NASA TN D-5399, Oct. 1969.

[22]Gielis, J., "A Generic Geometric Transformation that Unifies a Wide Range of Natural and Abstract Shapes," *American Journal of Botany*, Vol. 90, No. 3, 2003, pp. 333–338.

[23]Sabean, J. W., "Optimization of a Hypersonic Inlet with a Rectangular to Circular Transition Duct," Ph.D. Dissertation, Dept. of Aerospace Engineering, UM-AERO 99-09, Univ. of Maryland, College Park, MD, 1999.

[24]Anderson, J. D., *Hypersonic and High Temperature Gas Dynamics*, AIAA, Reston, VA, 2000, Chap. 3.

[25]Anderson, J. D., *Fundamentals of Aerodynamics*, 3rd ed., McGraw–Hill, New York, 2001, Chap. 8.

[26]Moseley, W. C., Jr., Moore, R. H., Jr., and Hughes, J. E., "Stability Characteristics of the Apollo Command Module," NASA TN D-3890, March 1967.

[27]Moseley, W. C., Jr., Graham, R. E., and Hughes, J. E., "Aerodynamic Stability Characteristics of the Apollo Command Module," NASA TN D-4688, Aug. 1968.

[28]DeRose, C. E., "Trim Attitude, Lift and Drag of the Apollo Command Module with Offset Center-of-Gravity Positions at Mach Numbers to 29," NASA TN D-5276, June 1969.

[29]Horstman, C. C., and Kussoy, M. I., "Free-Flight Measurements of Aerodynamic Viscous Effects on Lifting Re-Entry Bodies," *Journal of Spacecraft and Rockets*, Vol. 4, No. 8, 1967, pp. 1064–1069.

[30]DOT, Design Optimization Tools, Software Package, Ver. 4.20, Vanderplaats Research and Development, Inc., Colorado Springs, CO, 1995.

[31]Nelson, R. C., *Flight Stability and Automatic Control,* 2nd ed., McGraw–Hill, New York, 1997, Chaps. 1, 2.

[32]Micol, J. R., and Wells, W. L., "Hypersonic Lateral and Directional Stability Characteristics of Aeroassist Flight Experiment Configuration in Air and CF_4," NASA TN 4435, May 1993.

[33]Wells, W. L., "Measured and Predicted Aerodynamic Coefficients and Shock Shapes for Aeroassist Flight Experiment (AFE) Configuration," NASA TP-2956, Jan. 1990.

R. Cummings
Associate Editor